

Comparison of [^{11}C]UCB-J and [^{18}F]FDG PET in Alzheimer's disease: A tracer kinetic modeling study

Journal of Cerebral Blood Flow & Metabolism
2021, Vol. 41(9) 2395–2409
© The Author(s) 2021
Article reuse guidelines:
sagepub.com/journals-permissions
DOI: 10.1177/0271678X211004312
journals.sagepub.com/home/jcbfm



Ming-Kai Chen¹, Adam P Mecca², Mika Naganawa¹ , Jean-Dominique Gallezot¹, Takuya Toyonaga¹, Jayanta Mondal¹ , Sjoerd J Finnema¹ , Shu-fei Lin¹, Ryan S O'Dell², Julia W McDonald², Hannah R Michalak², Brent Vander Wyk², Nabeel B Nabulsi¹ , Yiyun Huang¹, Amy FT Arnsten², Christopher H van Dyck² and Richard E Carson¹

Abstract

[^{11}C]UCB-J PET for synaptic vesicle glycoprotein 2 A (SV2A) has been proposed as a suitable marker for synaptic density in Alzheimer's disease (AD). We compared [^{11}C]UCB-J binding for synaptic density and [^{18}F]FDG uptake for metabolism (correlated with neuronal activity) in 14 AD and 11 cognitively normal (CN) participants. We assessed both absolute and relative outcome measures in brain regions of interest, i.e., K_1 or R_1 for [^{11}C]UCB-J perfusion, V_T (volume of distribution) or DVR to cerebellum for [^{11}C]UCB-J binding to SV2A; and K_i or K_iR to cerebellum for [^{18}F]FDG metabolism. [^{11}C]UCB-J binding and [^{18}F]FDG metabolism showed a similar magnitude of reduction in the medial temporal lobe of AD –compared to CN participants. However, the magnitude of reduction of [^{11}C]UCB-J binding in neocortical regions was less than that observed with [^{18}F]FDG metabolism. Inter-tracer correlations were also higher in the medial temporal regions between synaptic density and metabolism, with lower correlations in neocortical regions. [^{11}C]UCB-J perfusion showed a similar pattern to [^{18}F]FDG metabolism, with high inter-tracer regional correlations. In summary, we conducted the first *in vivo* PET imaging of synaptic density and metabolism in the same AD participants and reported a concordant reduction in medial temporal regions but a discordant reduction in neocortical regions.

Keywords

SV2A, PET, [^{18}F]FDG, Synaptic Density, Alzheimer's disease

Received 16 October 2020; Revised 29 January 2021; Accepted 21 February 2021

Introduction

Positron emission tomography (PET) brain imaging with specific radiotracers has been used to evaluate biomarkers for Alzheimer's disease (AD) under the current AT(N) research framework,^{1,2} including [^{11}C]PiB and F-18 labeled amyloid PET for β -amyloid,^{3,4} tau PET for neurofibrillary tangles,^{5,6} and ^{18}F -fluorodeoxyglucose ([^{18}F]FDG) for glucose metabolism (correlated with neuronal activity) and neurodegeneration.⁷ Structural MRI for gray matter volume has also been widely used as a biomarker of neurodegeneration in AD.^{1,2} Although the relationship between structural gray matter volume and [^{18}F]FDG metabolism for functional neuronal activity has been well investigated

in AD,^{8–10} direct *in vivo* PET imaging and quantification of synaptic density in comparison with neuronal activity has never been reported. PET imaging for quantification of synaptic density was recently

¹Department of Radiology and Biomedical Imaging, Yale University School of Medicine, New Haven, CT, USA

²Department of Psychiatry, Yale University School of Medicine, New Haven, CT, USA

Corresponding author:

Ming-Kai Chen, Department of Radiology and Biomedical Imaging, Yale University School of Medicine, P.O. Box 208048, New Haven, CT 06520, USA.

Email: ming-kai.chen@yale.edu

developed as another potential biomarker for neurodegeneration in AD.^{11,12} Importantly, the ability to quantify synaptic density and neuronal activity in the same participants has the potential to provide a better understanding of AD pathophysiology. Here we conducted the first PET study with biomarkers for both synaptic density and glucose metabolism in the same AD participants. Because a discrepancy exists between regional brain atrophy and hypometabolism in AD,^{8–10} we hypothesized that the patterns of synaptic density loss and neuronal function in the susceptible regions of AD, including medial temporal lobe and posterior neocortical regions, would not be identical.

[¹⁸F]FDG brain PET is widely used for clinical differential diagnosis of dementia,^{13,14} and for tracking AD progression.^{15,16} [¹⁸F]FDG PET has also been used as a biomarker outcome measure for evaluation of treatment responses in many clinical trials of AD.^{17,18} Despite its frequent use as a surrogate marker of neuronal activity for neurodegeneration,⁷ [¹⁸F]FDG PET has its limitations. Because brain [¹⁸F]FDG uptake is often affected by sensory stimulation, medications, and blood glucose,^{19–22} the reproducibility of [¹⁸F]FDG PET quantification within and between participants can be affected by the difference of fasting status, current medications, and surrounding environmental stimulation of the participants.^{23–25} The appropriate preparation for the subjects before and during PET scanning is critical. Inadequate fasting could result in false positives in AD scans.^{21,22} These limitations in precision may ultimately hinder accurate assessment of disease progression or therapeutic effects in longitudinal clinical trials using [¹⁸F]FDG PET.

A potential imaging biomarker for synaptic density is the synaptic vesicle glycoprotein 2 A (SV2A), located in synaptic vesicles in presynaptic terminals and expressed in virtually all synapses.^{26,27} SV2A has a conserved expression pattern of about five copies per vesicle.²⁸ [¹¹C]UCB-J PET has been recently demonstrated as an excellent imaging agent for SV2A and has been applied in AD^{11,12} and other neuropsychiatric disorders.^{29–31} We have previously reported a low test-retest variability (3–9%) of [¹¹C]UCB-J V_T across all brain regions in the same human participants,³² and have also observed that [¹¹C]UCB-J PET V_T for synaptic density is stable in the presence of blood flow changes as with those accompanying visual stimulation.³³ This excellent reproducibility and non-stimulation-dependent quantification of [¹¹C]UCB-J PET could potentially be advantageous for use in longitudinal studies and clinical trials. Of note, most of the previous analyses for [¹¹C]UCB-J PET studies including our first study in early AD¹¹ were conducted using white matter (WM) in the centrum semiovale (CS) as the reference region.^{34–36} WM has the lowest total [¹¹C]

UCB-J binding with minimal SV2A specific binding and could therefore be a suitable reference region. However, the degree of [¹¹C]UCB-J uptake in WM could be variable, especially in those elderly subjects with WM pathology. Also, larger inter-subject variability from the use of a WM reference region could be a potential disadvantage. Using the regional ratios of distribution volume ($DVRs$) with the cerebellum as an alternative reference region, our substantially larger follow-up study of AD demonstrated widespread statistically significant reductions of SV2A binding in broader neocortical regions in addition to the hippocampus and entorhinal cortex in AD compared to cognitive normal (CN) participants.¹² These findings better reflect the pathologic findings of reduced cortical synaptic density in AD post mortem studies.³⁷ Therefore, we will continue using regional $DVRs$ to Cb as primary outcome measures of [¹¹C]UCB-J binding.

In the present study, we conducted [¹¹C]UCB-J dynamic PET scans with arterial input function for kinetic modeling and [¹⁸F]FDG PET in the same AD and CN participants. We computed multiple outcome measures from both [¹¹C]UCB-J PET and [¹⁸F]FDG PET to compare absolute and relative measures for better differentiating AD from CN, both in terms of regional percentage differences (PD) and standardized effect sizes with Cohen's *d*. Because absolute measures often have higher inter-subject variability, normalized measures could provide higher sensitivity for detecting group differences. We also explored the intra-regional associations between [¹¹C]UCB-J binding for synaptic density and [¹⁸F]FDG metabolism in the same participants to better understand their relationships in AD pathophysiology. In addition, our previous exploratory K_1 (indicating blood flow and tracer extraction) parametric imaging of [¹¹C]UCB-J demonstrated broad regional differences in temporoparietal cortices of AD relative to CN¹¹ that are similar to the known hypometabolic pattern of AD. Therefore, we also investigated whether K_1 parametric imaging of [¹¹C]UCB-J could serve as a surrogate for brain perfusion and provide similar information to [¹⁸F]FDG metabolism.

Materials and methods

Human participants

Fourteen participants with AD dementia or amnesic MCI due to AD and 11 CN participants enrolled in the study using the same methods as described previously¹¹ with more comprehensive details provided in the supplemental material. All participants received a PET scan with [¹¹C]Pittsburgh Compound B ([¹¹C]PiB) first to determine the presence of brain amyloid- β ($A\beta$) accumulation as previously described.¹¹ CN

participants who were negative for amyloid, and AD dementia or amnesic MCI due to AD participants who were positive for amyloid were included in the study. The study was approved by the Yale University Human Investigation Committee and the Radioactive Drug Research Committee and was conducted in accordance with the World Medical Association Declaration of Helsinki. All participants provided written informed consent prior to participating in the study.

PET imaging experiments

[¹¹C]UCB-J was synthesized according to previously described procedures.³⁵ All participants received [¹¹C]UCB-J and [¹⁸F]FDG dynamic PET measurement with the Siemens High Resolution Research Tomograph (HRRT; Siemens, Medical Solutions, Knoxville, TN, USA). The [¹¹C]UCB-J PET was performed as described previously¹¹ with details provided in the supplemental material. The [¹⁸F]FDG dynamic PET was also performed up to 90 min using the same acquisition protocol.

Quantitative analysis

For [¹¹C]UCB-J, kinetic analysis was performed voxel-by-voxel using the one-tissue compartment model (1TC)³² and the metabolite-corrected arterial plasma curve to generate a parametric image of distribution volume (V_T). V_T is the tissue:plasma concentration ratio at equilibrium and serves as an index of SV2A density and is not dependent on blood flow. Parametric images of the delivery rate constant, K_1 , which is proportional to blood flow ($K_1 = \text{flow} \times \text{extraction fraction}$), as well as R_1 , the ratio of regional K_1 values normalized to cerebellum (Cb) K_1 (i.e., $K_{1 \text{ ROI}}/K_{1 \text{ Cb}}$) were also produced. R_1 has lower inter-subject variability than K_1 and could serve as an important outcome measure for flow. Regions of interest (ROIs) were applied to the parametric images using the combined transformations from AAL template to PET space according to previous methods.¹¹ Additionally, distribution volume ratios ($DVRs$) for the ROIs using Cb as reference region were also calculated (i.e., $V_{T, \text{ROI}}/V_{T, \text{Cb}}$), derived directly from the 1TC parameters using arterial input function (AIF) as the gold standards, not from reference-region based analysis e.g. simplified reference tissue model 2 (SRTM2). We have previously demonstrated an excellent correlation between DVR values derived from 1-TC parameters with AIF and from SRTM2 (see supplemental materials from our recent paper).¹² Therefore, the DVR findings in the current study can be extended to reference region methods.

For [¹⁸F]FDG, Patlak analysis³⁸ was performed according to the methods described previously with modification, with t^* set to 60 min and a 30-min scan duration was used to measure the influx rate constant K_i for each ROI. The net influx constant K_i is a commonly used outcome measure for cerebral glucose metabolism.³⁸ A population-based input function (PBIF) was used for the analysis,³⁹ which has been validated recently as a suitable alternative to the AIF. Briefly, the PBIF was generated from the averages of arterial plasma curves (in SUV units) from 40 participants (not included in this study). To scale the PBIF, venous plasma samples were acquired for each participant in this study. The PBIF was scaled by the ratio of the mean venous plasma SUV value to the mean PBIF between 40 and 60 minutes. The ratio of regional K_i values (K_iR) for the ROIs using Cb as reference region were also calculated (i.e., $K_iR = K_{i \text{ ROI}}/K_{i \text{ Cb}}$).

Gray matter tissue loss can affect PET measures. To minimize this, we masked the ROIs with a segmented MRI (gray matter masking)⁴⁰ and performed full partial volume correction (PVC) using Muller-Gardner method (M-G).^{41,42} DVR , R_1 and K_iR after PVC were calculated using non-PVC Cb as reference region.

Statistical analysis

Statistical calculations were performed in Microsoft Excel 2016, IBM SPSS (version 26) and GraphPad PRISM (version 8). When comparing the group differences between tracers, the % difference of the means and Cohen's d are listed as (PD:x%/d:x). Separate linear mixed models were used to compare each parameter of [¹¹C]UCB-J (K_1 , R_1 , V_T , DVR) or [¹⁸F]FDG (K_i , K_iR) before or after PVC in 16 regions (within-subject factor) between AD and CN groups. A random intercept was included and the best-fitting variance-covariance structure was compound symmetry as determined by the Bayesian information criterion. Since the goal of this study is the comparison of [¹¹C]UCB-J and [¹⁸F]FDG, we chose to assess the ability to detect group differences without including the effects of age, sex and education. Post-hoc comparisons utilized unpaired t -tests (2-tailed and $P < 0.05$ for significance). In addition, the Benjamini-Hochberg procedure was used to control the false discovery rate for multiple comparisons. Standardized effect sizes with Cohen's d were also calculated for the binding parameters of both tracers in each ROI between AD and CN groups. Correlation between the binding parameters of [¹¹C]UCB-J and [¹⁸F]FDG within each region was performed with Pearson correlation coefficients. The modified version of the Pearson-Filon statistical test,⁴³ which accounts for non-independent data, was used to compare inter-tracer correlations between regions and the differences

of correlations before and after PVC; significance was based on a two-tailed test, with $P < 0.05$.

Results

Participants characteristics

Fourteen individuals with amnesic MCI or dementia due to AD and 11 CN individuals participated in the study. Diagnostic groups were well balanced for age

Table 1. Demographic information and test results of included participants.

	Cognitively normal (CN)	Alzheimer's disease (AD)
Participants	11	14 (mild AD:4, MCI: 10)
Sex (M/F)	3/8	7/7
Age (years)	69.4 (9.0) (59–81)	69.6 (5.7) (58–79)
Education (years)	17.5 (2.5) (12–20)	16.9(1.8) (13–19)
CDR-global	0 (0)	0.6 (0.2) (0.5–1)
CDR-sb	0 (0)	2.9 (1.5) (0.5–4.5)
MMSE	29.0 (1.2) (27–30)	23.9 (4.6) (14–29)
LMII	13.1 (5.5) (5–19)	2.4 (2.8) (0–8)
RAVLT	11.1(3.0) (6–14)	2.2 (2.6) (0–9)

Data are n, or mean (SD) (range).

CDR-global: clinical dementia rating global score; CDR-sb: clinical dementia rating sum of boxes; MMSE: Mini-Mental State Examination; LMII: Logical Memory II score; RAVLT: Rey Auditory Verbal Learning Test delayed recall.

and education (Table 1). AD participants had clinical characteristics typical of amnesic MCI and mild dementia with $MMSE = 23.9 \pm 4.6$ and $CDR = 0.6 \pm 0.2$. All participants received one injection of [^{11}C]UCB-J (604 ± 188 MBq and mass 1.60 ± 0.97 μg) and one injection of [^{18}F]FDG (181 ± 6 MBq) with no significant difference in injection doses and masses between groups. The average time differences between the two scans were 6 ± 27 days for AD and 114 ± 136 days for CN participants, respectively. For [^{11}C]UCB-J, the arterial input functions were successfully measured in all participants to measure K_1 , R_1 (to Cb), V_T , and DVR (to Cb). For [^{18}F]FDG, the PBIF was used to measure K_i and K_iR (to Cb).

Regional synaptic loss and hypometabolism in AD

When comparing [^{11}C]UCB-J binding and [^{18}F]FDG metabolism, the regional pattern of lower [^{11}C]UCB-J binding (V_T , DVR) was different from that of hypometabolism (K_i , K_iR) observed in AD participants. Typical AD images are shown in Figure 1. Our visual inspection of images revealed lower uptake of both [^{11}C]UCB-J and [^{18}F]FDG in the medial temporal lobe for the same AD participants, but we observed more pronounced reductions of [^{18}F]FDG uptake in the lateral temporal lobe, the parietal lobe, and the posterior cingulate. Since there were no disease-specific effects in the cerebellum (Table S1), [^{11}C]UCB-J V_T and [^{18}F]FDG K_i were normalized to

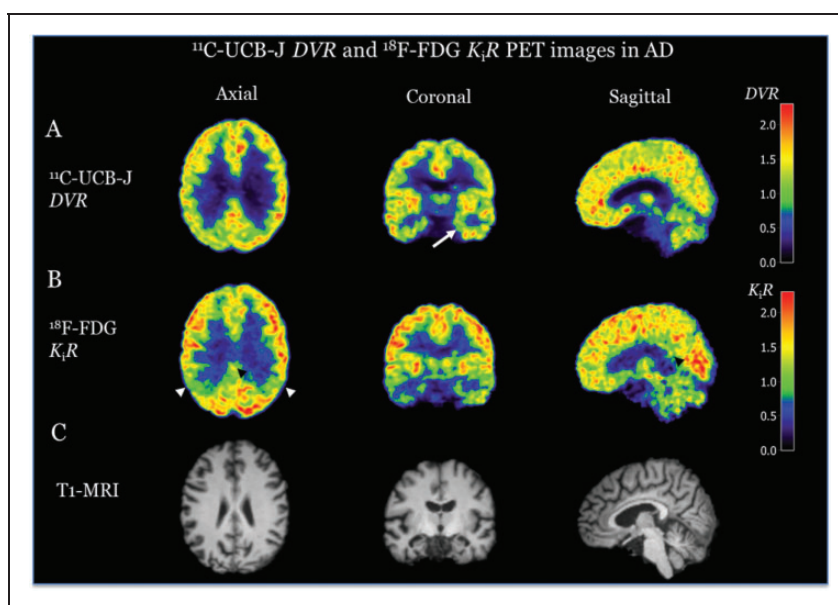


Figure 1. Representative (A) [^{11}C]UCB-J DVR and (B) [^{18}F]FDG PET K_iR images and (C) MRI images in AD. Evident lower [^{11}C]UCB-J binding in the hippocampus of AD was noted (arrow denotes the left hippocampus). Evident hypometabolism was also noted in the hippocampus of AD. In addition, hypometabolism was also noted in lateral temporal and parietal cortices of AD (white arrows denote the parietal cortices) as well as posterior cingulate (black arrow heads).

Table 2. Comparison of [¹¹C]UCB-J DVR and [¹⁸F]FDG K_iR in the ROIs of AD and CN.

Region	[¹¹ C]UCB-J DVR				[¹⁸ F]FDG K _i R				
	CN (n = 11) Mean (%SD)	AD (n = 14) Mean (%SD)	P	Cohen's d	CN (n = 11) Mean (%SD)	AD (n = 14) Mean (%SD)	PD	P	Cohen's d
Hippocampus	1.01 (7%)	0.76 (21%)	<0.0001*†	1.93	0.91 (10%)	0.70 (19%)	23.4%	<0.0001*†	1.89
Entorhinal	1.16 (8%)	0.89 (23%)	0.0003*†	1.62	0.80 (15%)	0.60 (23%)	24.4%	0.001*†	1.50
Amygdala	1.38 (9%)	1.15 (20%)	0.003*†	1.25	0.87 (13%)	0.69 (20%)	20.2%	0.002*†	1.39
Parahippocampus	1.10 (8%)	0.94 (14%)	0.001*†	1.44	0.88 (10%)	0.74 (15%)	15.4%	0.003*†	1.29
Precuneus	1.45 (8%)	1.33 (13%)	0.044*	0.82	1.66 (9%)	1.34 (21%)	19.2%	0.002*†	1.36
Post. Cingulate	1.01 (18%)	0.90 (25%)	0.188	0.53	1.36 (16%)	1.05 (21%)	22.7%	0.002*†	1.39
Angular	1.46 (6%)	1.33 (13%)	0.025*†	0.91	1.59 (8%)	1.20 (27%)	24.6%	0.001*†	1.53
Parietal	1.41 (8%)	1.29 (13%)	0.040*†	0.84	1.55 (11%)	1.28 (21%)	17.4%	0.005*†	1.18
Temporal	1.44 (5%)	1.33 (9%)	0.012*†	1.04	1.33 (8%)	1.10 (18%)	16.8%	0.002*†	1.31
Ant. Cingulate	1.34 (9%)	1.23 (18%)	0.106	0.64	1.16 (11%)	1.02 (18%)	12.2%	0.033*†	0.88
Caudate	1.09 (16%)	0.96 (14%)	0.052	0.87	1.11 (16%)	0.93 (16%)	16.5%	0.014*†	1.12
Frontal	1.35 (7%)	1.27 (9%)	0.084	0.71	1.54 (8%)	1.30 (15%)	15.2%	0.001*†	1.39
Occipital	1.38 (8%)	1.33 (10%)	0.335	0.39	1.49 (10%)	1.33 (19%)	10.6%	0.063	0.74
Pulvinar	1.14 (11%)	0.93 (15%)	0.001*†	1.55	1.14 (14%)	0.94 (16%)	17.3%	0.005*†	1.26
Putamen	1.60 (9%)	1.58 (8%)	0.716	0.15	1.67 (11%)	1.54 (11%)	8.2%	0.062	0.80
Thalamus	1.03 (10%)	0.90 (11%)	0.005*†	1.28	1.26 (11%)	1.13 (12%)	10.5%	0.028*†	0.95

Data are mean (%SD/covariance) of ROI values normalized to cerebellum. P-values are for post hoc two-tailed, unpaired t-tests (uncorrected for multiplicity) performed after a linear mixed model analysis of [¹¹C]UCB-J DVR and [¹⁸F]FDG K_iR in multiple regions (within-subject factor) between CN and AD groups. PD is the percentage difference in the group means; 100(CN-AD)/CN.

*p < 0.05 prior to false discovery rate correction for multiple comparisons. †p < 0.05 after false discovery rate correction.

Please note the regions in this table as well as the supplement tables are partitioned in the same fashion, including medial temporal regions (Hippocampus, Entorhinal, Amygdala, Parahippocampus), susceptible neocortical regions (Precuneus, Post. Cingulate, Angular, Parietal, and Temporal), other brain regions (Ant. Cingulate, Caudate, Frontal, Occipital, Pulvinar, Putamen, Thalamus).

CN: cognitively normal; AD: Alzheimer's disease.

cerebellum to yield DVR and K_iR , respectively. We observed a similar pattern of lower $[^{11}C]UCB-J$ DVR and $[^{18}F]FDG$ K_iR in AD participants with larger effect sizes (Table 2) when compared to the unnormalized values (Table S1). We found similar between-group differences and increased effect sizes in $[^{11}C]UCB-J$ DVR and $[^{18}F]FDG$ K_iR in the medial temporal regions (Table 2). Significant between-group differences of $[^{11}C]UCB-J$ DVR were also present in the putamen with slightly larger effect sizes than $[^{18}F]FDG$ K_iR (Table 2). With the improved effect sizes after cerebellum normalization, we were able to detect small between-group differences of $[^{11}C]UCB-J$ DVR in susceptible neocortical regions that were less than the PD of $[^{18}F]FDG$ K_iR (Table 2). The regional relationships

are plotted showing the percent differences in mean value (AD vs. CN) in Figure 2(c) and the Cohen's d for differentiation between AD and CN in Figure 2(d). Comparing $[^{11}C]UCB-J$ DVR and $[^{18}F]FDG$ K_iR demonstrated overall similar PD in medial temporal regions, but lower PD of $[^{11}C]UCB-J$ DVR in the neocortical regions. ROIs to the lower right of the identity line reflect greater difference/Cohen's d for $[^{11}C]UCB-J$, whereas those to the upper left indicate greater difference/Cohen's d for $[^{18}F]FDG$.

The linear mixed model analysis (LMMA) demonstrated a significant group effect ($F(1,23)=15.4$, $p=0.001$) and group*region ($F(15,345)=2.2$, $p=0.007$) for $[^{11}C]UCB-J$ DVR . Post-hoc comparisons showed significantly lower $[^{11}C]UCB-J$ DVR in medial temporal and thalamic

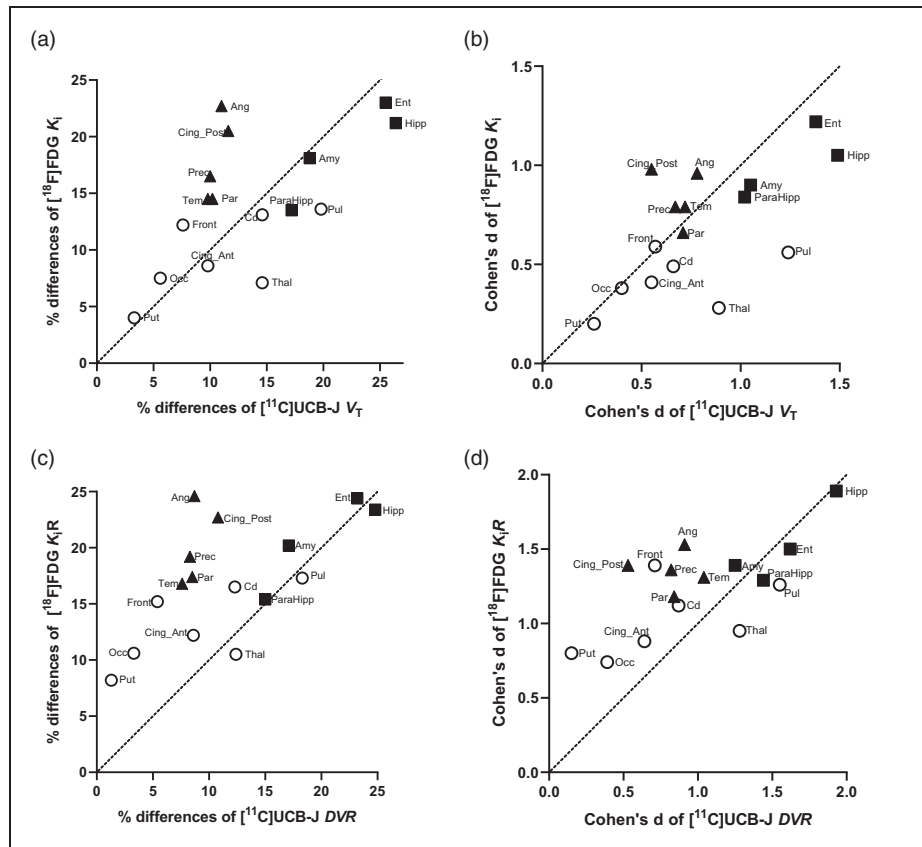


Figure 2. Scatter plots of regional percentage differences of means between CN and AD (a, c) and Cohen's d (b, d) for $[^{11}C]UCB-J$ (V_T and DVR on x-axis) versus $[^{18}F]FDG$ (K_i and K_iR on y-axis). (a) Comparing $[^{11}C]UCB-J$ V_T and $[^{18}F]FDG$ K_i demonstrated distinct patterns, including slightly higher % differences of $[^{11}C]UCB-J$ V_T in medial temporal regions (■ Hipp, Ent, Amy, and ParaHipp) and thalamic regions, but smaller % differences in susceptible neocortical regions (▲ Ang, Cing_Post, Prec, Tem, Par). (b) There were larger Cohen's d values for $[^{11}C]UCB-J$ V_T vs. $[^{18}F]FDG$ K_i in medial temporal regions and thalamic regions (○ Thal and Pul), but slightly lower Cohen's d values in susceptible neocortical regions. (c) Comparing $[^{11}C]UCB-J$ DVR and $[^{18}F]FDG$ K_iR demonstrated overall similar % differences in medial temporal regions, but lower % differences of $[^{11}C]UCB-J$ DVR in the susceptible neocortical and other examined regions (symbol ○). (d) Higher Cohen's d values for $[^{11}C]UCB-J$ DVR vs $[^{18}F]FDG$ K_iR in some medial temporal regions (■ Hipp and Ent) and thalamic regions, but overall lower Cohen's d values in $[^{11}C]UCB-J$ DVR in other examined regions. Amy: Amygdala; Ang: angular; CS: centrum semiovale; Cd: Caudate; Cing_Ant: Ant. Cingulate; Cing_Post: Post. Cingulate; Ent: Entorhinal; Front: Frontal; Hipp: Hippocampus; Occ: Occipital, ParaHipp: ParaHippocampus; Par: Parietal; Prec: Precuneus; Pul: Putamen; Tem: Temporal; Thal: Thalamus.

regions, and some neocortical regions after adjustment for multiple comparisons (Table 2). The LMMA also demonstrated a significant group effect ($F(1,23)=18.9$, $p<0.001$) and group*region ($F(15,345)=1.9$, $p=0.019$) for [^{18}F]FDG K_iR . Post-hoc comparisons revealed significantly lower [^{18}F]FDG K_iR in all medial temporal, thalamic and neocortical regions after adjustment for multiple comparisons (Table 2).

When comparing absolute kinetic values, i.e., [^{11}C]UCB-J V_T with [^{18}F]FDG K_i , we detected slightly larger between-group differences for [^{11}C]UCB-J V_T in the medial temporal regions with higher effect sizes (Supplemental Table S1). We also found slightly larger between-group differences of [^{11}C]UCB-J V_T in the thalamic regions (thalamus and pulvinar). However, unlike [^{18}F]FDG, [^{11}C]UCB-J V_T demonstrated no significant between-group differences in susceptible neocortical regions (Table S1). These regional values for the two tracers are also plotted, showing the between-group PD in Figure 2(a) and the Cohen's d in Figure 2(b).

The LMMA demonstrated a significant group effect ($F(1,23)=5.6$, $p=0.027$) and group*region interaction ($F(15,345)=2.1$, $p=0.008$) for [^{11}C]UCB-J V_T . Post-hoc comparisons revealed significant group differences of [^{11}C]UCB-J V_T in the hippocampus, entorhinal, amygdala, and pulvinar after adjustment for multiple comparisons (Table S1). Note that LMMA demonstrated no significant effect of group ($F(1,23)=3.5$, $p=0.07$) or group*region interaction ($F(15,345)=1.5$, $p=0.09$) for [^{18}F]FDG K_i and no significant between-group differences in the examined regions after adjustment for multiple comparisons (Table S1).

Regional hypoperfusion and hypometabolism in AD

Comparing [^{11}C]UCB-J K_1 for perfusion and [^{18}F]FDG K_i for metabolism, as potential surrogate measures of neuronal activity, we found a similar regional pattern and degree of group differences for both parameters, consistent with lower perfusion and metabolism in AD (Tables S1 and S2). The regional relationships are plotted showing the PDs in mean value (AD vs. CN) in Figure 3(a) and the Cohen's d in Figure 3(b). Note that LMMA demonstrated close to significant group effect ($F(1,23)=4.2$, $p=0.05$) but no group*region interaction ($F(15,345)=1.3$, $P=0.2$) for [^{11}C]UCB-J K_1 . Post-hoc comparisons only revealed significant [^{11}C]UCB-J K_1 differences in the hippocampus and entorhinal cortex of AD compared to CN after adjustment for multiple comparisons (Table S3).

With no group differences in cerebellum, [^{11}C]UCB-J K_1 and [^{18}F]FDG K_i were normalized to cerebellum to yield R_1 and K_iR , respectively. We observed a similar pattern of lower values of both [^{11}C]UCB-J R_1 (Table

S2) and [^{18}F]FDG K_iR (Table 2) in AD participants with higher effect sizes and statistical significance than the unnormalized values. These findings are illustrated in Figures 3(c) and (d) with the shift of the examined regions. The shift of PD values is probably due to the slight differences in reference cerebellum values. The LMMA for [^{11}C]UCB-J R_1 demonstrated a significant effect of group ($F(1,23)=10.5$, $p=0.004$) but no significant group*region interaction ($F(15,345)=1.6$, $P=0.066$). Post-hoc comparisons revealed significantly lower [^{11}C]UCB-J R_1 in AD compared to CN participants in all medial temporal, thalamic and neocortical regions after adjustment for multiple comparisons (Table S2).

Partial volume correction

We also performed PVC for correction of brain atrophy and gray-white spill-in. PVC was associated with an overall decrease in statistical significance and the effect sizes for most regions (Tables S3–5). Statistically significant group differences remained for [^{11}C]UCB-J DVR in the hippocampus and the pulvinar after PVC (Table S4). Using the K_iR of [^{18}F]FDG after PVC, there were larger and significant between-group differences and more statistically significant regions than using [^{11}C]UCB-J DVR after PVC (Table S4).

Regional correlations between synaptic density and metabolism

We explored inter-tracer correlations between the regional measures of [^{11}C]UCB-J (K_1 , R_1 , V_T , DVR), and [^{18}F]FDG (K_i and K_iR) across participants. For the relationship between [^{11}C]UCB-J binding (V_T , DVR) and [^{18}F]FDG metabolism (K_i and K_iR), various degrees of correlation emerged between the two tracers among the examined regions, particularly in medial temporal and susceptible neocortical regions (Table S6). We selected hippocampus as the representative of medial temporal regions for demonstration purpose because we found the highest inter-group PD and Cohen's d of [^{11}C]UCB-J bindings within this region (Figure 2). We also selected precuneus as the representative of susceptible neocortical regions for demonstration because it is considered a vulnerable region of hypometabolism in AD and is characterized by less inter-subject variability than posterior cingulate (Table 2). Higher correlations were noted between [^{11}C]UCB-J DVR and [^{18}F]FDG K_iR compared to those between [^{11}C]UCB-J V_T and [^{18}F]FDG K_i in the same regions (Figure 4(a) and (b)). Overall, the correlations between [^{11}C]UCB-J DVR and [^{18}F]FDG K_iR in the medial temporal regions were significantly higher than those in the susceptible neocortical regions.

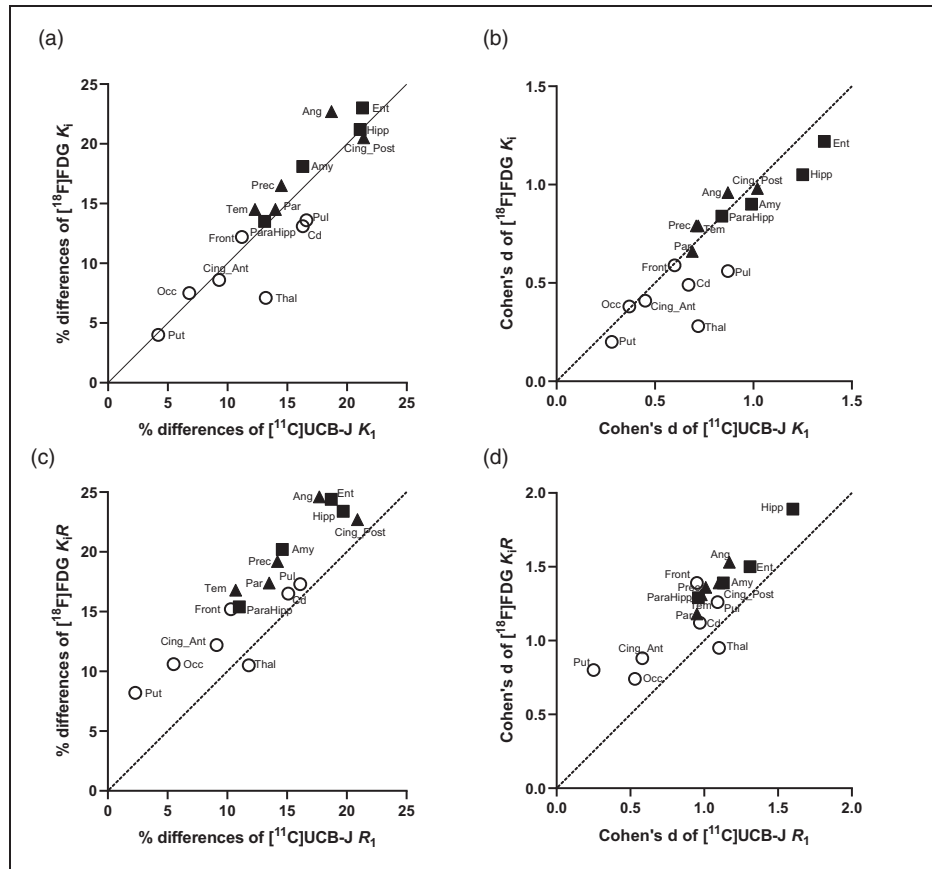


Figure 3. Scatter plots of regional percentage differences between CN and AD (a, c) and Cohen's *d* (b, d) for [^{11}C]UCB-J (K_1 and R_1 on x-axis) versus [^{18}F]FDG (K_i and K_iR on y-axis). (a) Comparing [^{11}C]UCB-J K_1 and [^{18}F]FDG K_i demonstrated very similar % differences in most examined regions including in medial temporal regions (■ Hipp, Ent, Amy, and ParaHipp), susceptible neocortical regions (▲ Ang, Cing_Post, Prec, Tem, Par), and other examined regions (○), which appeared well aligned along the identity line. (b) There were similar Cohen's *d* values of [^{11}C]UCB-J K_1 vs [^{18}F]FDG K_i in most examined regions. (c) Comparing [^{11}C]UCB-J R_1 and [^{18}F]FDG K_iR demonstrated generally lower % differences of [^{11}C]UCB-J R_1 in the examined regions. (d) Overall, there were slightly lower Cohen's *d* values of [^{11}C]UCB-J R_1 vs [^{18}F]FDG K_iR in the examined regions.

Amy: Amygdala; Ang: angular; CS: centrum semiovale; Cd: Caudate; Cing_Ant: Ant. Cingulate; Cing_Post: Post. Cingulate; Ent: Entorhinal; Front: Frontal; Hipp: Hippocampus; Occ: Occipital; ParaHipp: ParaHippocampus; Par: Parietal; Prec: Precuneus; Pul: Pulvinar; Put: Putamen; Tem: Temporal; Thal: Thalamus.

For example, the correlation in the hippocampus ($R^2=0.86$) was higher than that in the precuneus ($R^2=0.59$) ($p=0.022$) (Figure 4(b)). We further performed inter-tracer correlations after PVC and found an overall decrease in correlations, as shown in Figure 4(c) and (d).

Regional correlations between perfusion and metabolism

For perfusion (K_1 and R_1) and metabolism (K_i and K_iR), the correlations between normalized measures ([^{11}C]UCB-J R_1 and [^{18}F]FDG K_iR) were overall very strong in the affected regions (medial temporal and neocortical regions) ($R^2 = 0.72-0.91$) and were higher than those between the absolute measures ([^{11}C]UCB-J K_1 and [^{18}F]FDG K_i) in the same regions ($R^2 = 0.21-$

0.66) (Table S6 and Figure 5(a) and (b)). We observed no significant regional differences in the correlations ([^{11}C]UCB-J R_1 vs [^{18}F]FDG K_iR) for the medial temporal and neocortical regions (e.g. $R^2=0.84$ in the hippocampus versus $R^2=0.85$ in the precuneus, $p=0.87$). We further performed inter-tracer correlations after PVC and found an overall decrease in correlations (Table S6 and Figure 5(c) and (d)).

Discussion

We conducted the first comparison study of absolute and normalized regional measures of [^{11}C]UCB-J binding for synaptic density and [^{18}F]FDG uptake for metabolism in the same AD and CN participants. The most important findings from this study are the distinct regional patterns of synaptic loss and

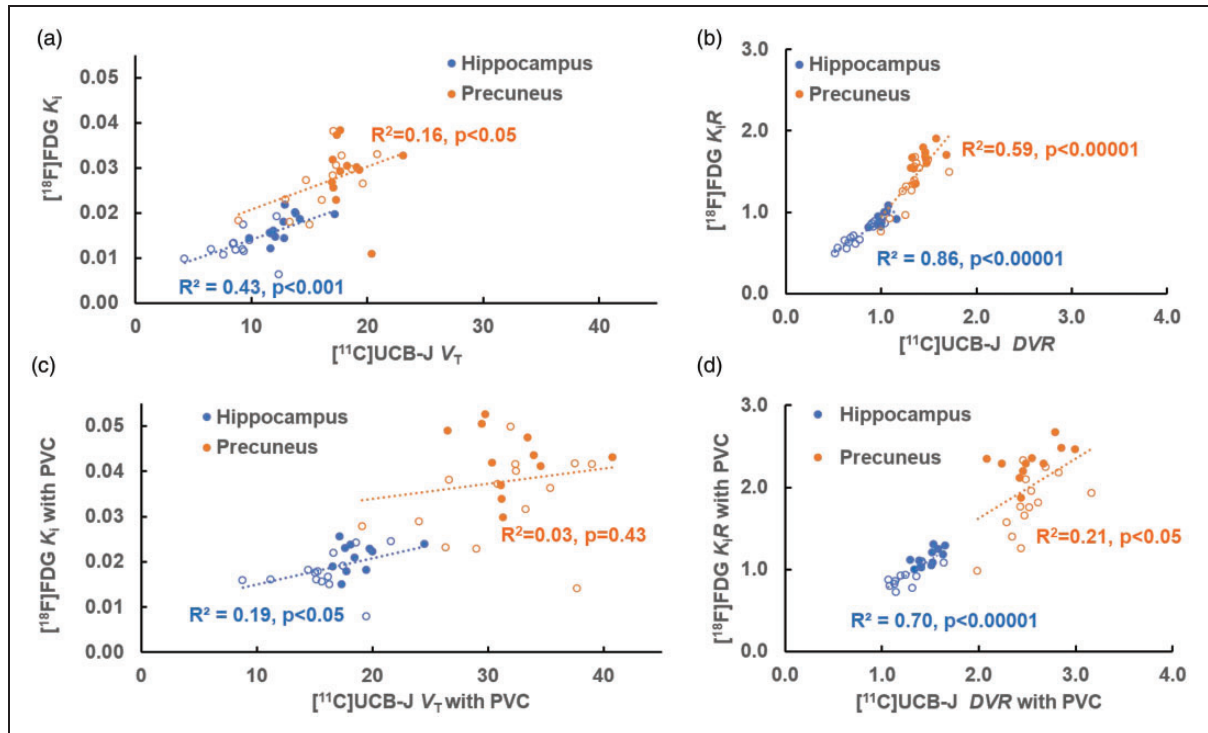


Figure 4. Scatter plots of regional $[^{11}\text{C}]\text{UCB-J}$ (V_T and DVR on x-axis) versus $[^{18}\text{F}]\text{FDG}$ (K_i and K_iR on y-axis) in the hippocampus and precuneus before (a & b) and after PVC (c & d). The solid circles indicate CN participants and the open circles indicate AD participants. (a) There were statistically significant correlations in the hippocampus ($R^2=0.43$) and in the precuneus ($R^2=0.16$) between $[^{11}\text{C}]\text{UCB-J } V_T$ and $[^{18}\text{F}]\text{FDG } K_i$. (b) After normalization to cerebellum, the correlations between $[^{11}\text{C}]\text{UCB-J } \text{DVR}$ and $[^{18}\text{F}]\text{FDG } K_iR$ increased with higher values in the hippocampus ($R^2=0.86$) and in the precuneus ($R^2=0.59$). (c) After PVC, the correlations between $[^{11}\text{C}]\text{UCB-J } V_T$ and $[^{18}\text{F}]\text{FDG } K_i$ were significantly lower in the hippocampus ($R^2=0.19$) and in the precuneus ($R^2=0.03$). (d) After normalization to cerebellum, the correlations between $[^{11}\text{C}]\text{UCB-J } \text{DVR}$ and $[^{18}\text{F}]\text{FDG } K_iR$ after PVC increased in the hippocampus ($R^2=0.70$) and in the precuneus ($R^2=0.21$).

hypometabolism in AD. Overall, we found similar degrees of synaptic loss and hypometabolism in medial temporal regions but a greater degree of hypometabolism than synaptic loss in the susceptible neocortical regions of AD (Table 2 and Figure 2). We also demonstrated overall significant correlations between $[^{11}\text{C}]\text{UCB-J}$ binding and $[^{18}\text{F}]\text{FDG}$ metabolism within the affected regions, with higher inter-tracer correlations in the medial temporal regions (e.g. hippocampus) than in the neocortical regions (e.g. precuneus) (Figure 4 and Table S6). These findings strongly indicate that synaptic loss and hypometabolism were concordant in the medial temporal regions but were discordant in the susceptible neocortical regions.

Divergence of synaptic density and metabolism in AD

Hypometabolism in the temporoparietal lobes, precuneus, and posterior cingulate gyrus is the classic signature of $[^{18}\text{F}]\text{FDG}$ PET in early AD,^{44,45} although this posterior neocortical pattern differs somewhat from known pathological findings of neurodegeneration

predominantly in medial temporal regions (entorhinal cortex and hippocampus) in early AD.^{9,46–48} In the current study, we did observe significantly lower $[^{11}\text{C}]\text{UCB-J}$ binding for synaptic density in the neocortical regions of AD (Table 2) consistent with our previous study¹² and known postmortem AD pathology.³⁷ However, the magnitude of AD hypometabolism exceeded that of synaptic loss in the association neocortices. Reasons for this divergence of synaptic density and metabolism in these regions are likely multifactorial and may include: incipient neurodegeneration within association neocortices, distant effects of neurodegeneration in the medial temporal lobes, and bioenergetic effects.

One possible explanation is disproportionate hypometabolism related to developing tau pathogenesis and neurodegeneration within the association neocortices that precedes synaptic loss in the direct projections to these regions. Although we did not perform tau PET imaging in the present study, a number of studies have reported strong correlations between regional tau

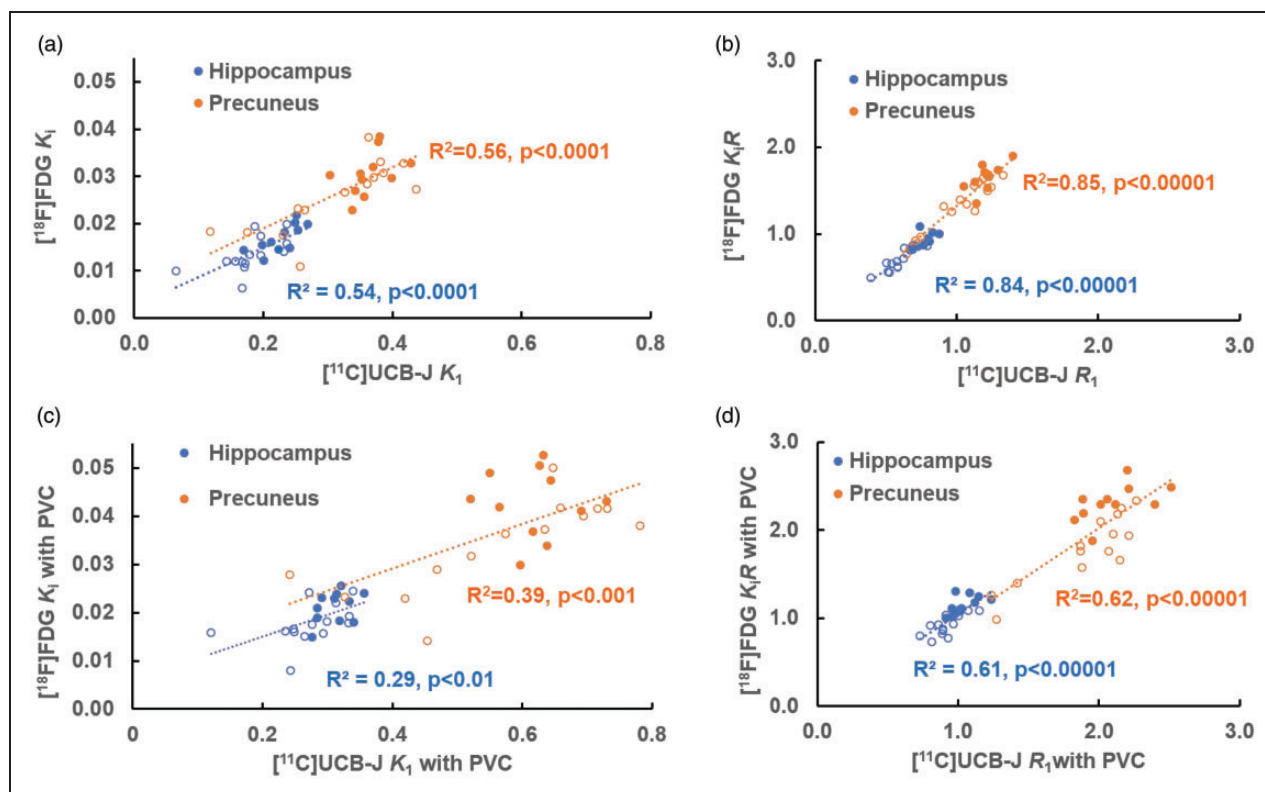


Figure 5. Scatter plots of regional $[^{11}\text{C}]\text{UCB-J}$ (K_i and R_i on x-axis) versus $[^{18}\text{F}]\text{FDG}$ (K_i and K_i/R on y-axis) in the hippocampus and precuneus before (a & b) and after PVC (c & d). The solid circles indicate CN participants and the open circles indicate AD participants. (a) There were similar statistically significant correlations between $[^{11}\text{C}]\text{UCB-J } K_i$ and $[^{18}\text{F}]\text{FDG } K_i$ in the hippocampus ($R^2=0.54$) and in the precuneus ($R^2=0.56$). (b) After normalization to cerebellum, the correlations between $[^{11}\text{C}]\text{UCB-J } R_i$ and $[^{18}\text{F}]\text{FDG } K_i/R$ increased with higher values in the hippocampus ($R^2=0.84$) and in the precuneus ($R^2=0.85$). (c) After PVC, the correlations between $[^{11}\text{C}]\text{UCB-J } K_i$ and $[^{18}\text{F}]\text{FDG } K_i$ were significantly lower in the hippocampus ($R^2=0.29$) and in the precuneus ($R^2=0.39$). (d) After normalization to cerebellum, the correlations between normalized $[^{11}\text{C}]\text{UCB-J } R_i$ and $[^{18}\text{F}]\text{FDG } K_i/R$ after PVC increased in the hippocampus ($R^2=0.61$) and in the precuneus ($R^2=0.62$).

deposition and hypometabolism^{49–52} and hypoperfusion.⁵³ Moreover, early tau accumulation with associated hypometabolism in neocortical regions may precede synaptic loss and SV2A reductions in the direct projections to these regions. Further multi-tracer studies, incorporating tau PET will be valuable to investigate this possibility.

The divergence of synaptic density and metabolism in association neocortex may also pertain to distant effects of medial temporal lobe degeneration. Discrepant patterns of hypometabolism and atrophy in AD have previously been noted^{9,46–48} and have been attributed partly to diaschisis^{9,46–48} (i.e. the occurrence of neurophysiological changes distant from a focal brain lesion⁵⁴) and/or indirect disconnection of association neocortices.⁹ Because neurodegeneration in entorhinal cortex and hippocampus is an early event in AD pathogenesis,^{55,56} it may be associated with hypometabolism in a number of projection regions, including temporoparietal cortex, posterior cingulate gyrus-precuneus, and orbito-medial frontal

areas.^{9,46–48} Additional credence for this explanation is provided by studies in a nonhuman primate model of AD, which reported hypometabolism in several posterior association cortices and posterior hippocampus following neurotoxic lesions to entorhinal and perirhinal cortices.⁵⁷ Early degeneration of the entorhinal and perirhinal cortices in AD likely produces a similar reduction in metabolism in these same structures. Although these posterior cortices receive multiple projections from other brain regions, the loss of excitatory inputs from medial temporal lobe may be sufficient to induce substantial hypometabolism without commensurate loss of synaptic density.

Yet another possible explanation for greater hypometabolism than synaptic loss in the neocortices of early AD is based on bioenergetics, whereby decreased glucose metabolism is an upstream event that precedes and results in the neuropathologic features of AD, including synaptic loss due to insufficient energy supply.^{7,58} Although $[^{18}\text{F}]\text{FDG}$ PET is sometimes used as a surrogate for synaptic activity, it also reflects

energy utilization by neurons and glia for a variety of functions.^{59–61} The direct measures of K_i simply indicate the influx of glucose for subsequent glycolysis. Moreover, impairments in astroglial transfer of glucose from the vasculature to neurons may contribute to metabolic deficits in AD^{59–61} and may be particularly harmful in watershed zones where blood supply is most limited. In this regard, it is noteworthy that the susceptible neocortical regions that show hypoperfusion and hypometabolism in AD lie in vulnerable watershed zones between the territories of the middle and posterior cerebral arteries,⁶² which could also explain the disproportionate hypometabolism relative to synaptic loss in those regions.

Lastly, the discrepancy between hypometabolism and SV2A reductions in the neocortical regions could be partly explained by compensatory synaptic reorganization in early stage of AD (see review Arendt 2009)⁶³ or increased synaptic contact size⁶⁴ (with increased SV2A per remaining synapse). Accumulations of SV2 has also been reported in dystrophic neurites within neuritic plaques that might obscure synaptic loss in amyloid-rich regions.⁶⁵ Nevertheless, the current study provides the first in vivo analysis of the relationship between synaptic density and glucose metabolism in the same AD participants. Further studies incorporating tau PET or post-mortem pathology may provide a better understanding of these issues.

Positive association of synaptic density and metabolism in AD

[¹⁸F]FDG brain PET for glucose metabolism is often utilized as a biomarker of neuronal and synaptic activity,⁷ presumed to be closely related to synaptic density, although direct in vivo evidence has been lacking. A previous study in a baboon demonstrated significant positive correlations between resting [¹⁸F]FDG PET and in vitro synaptophysin, a marker of synaptic density, across all the examined regions⁶⁶ and supported the hypothesis that glucose metabolism reflects integrated synaptic activity.⁶⁶ The current study provided the first evidence of significant positive correlations between in vivo SV2A PET for synaptic density and [¹⁸F]FDG PET for metabolism across susceptible regions for AD with higher inter-tracer correlations in the medial temporal regions and lower inter-tracer correlations in the neocortices (Figure 4 and Table S6). Although these inter-tracer correlations in the susceptible regions could be falsely amplified by brain atrophy, they persisted after PVC in the medial temporal regions. We also performed correlational analyses in CN and AD groups separately and found similar high inter-tracer correlations in the AD group, but not in the CN (data not shown), supporting the idea

of concordant synaptic loss and decreased neuronal function in the medial temporal lobe; although the lack of significant correlation in the CN group could also be due to the smaller dynamic range of values in this group. In contrast, lower or no significant inter-tracer correlations in the neocortices after PVC is likely due to discordant synaptic loss and decreased neuronal function as discussed above. While revising our manuscript, a recently published study of FDG and SV2A PET in 20 female young healthy subjects (age 29.6 ± 9.9 yrs) also showed an overall statistically significant correlation ($r > 0.47$, $p < 0.001$) between global measures of glucose metabolism at rest and synaptic density.⁶⁷ Interestingly, a substantial regional variation between glucose metabolism and synaptic density was also reported among the healthy young subjects,⁶⁷ although this may not be directly applicable to the current study with elderly and AD participants. Future investigation in a larger study is needed for better understanding of the relationships between regional glucose metabolism and synaptic density in AD.

Cerebral perfusion and metabolism in AD

The current study further supports the notion that K_1 and R_1 from dynamic [¹¹C]UCB-J PET imaging could serve as a surrogate for cerebral perfusion and could predict the pattern of [¹⁸F]FDG metabolism. Our recent study in healthy control participants showed that [¹¹C]UCB-J K_1 is highly sensitive to increased blood flow induced by visual stimulation, with no effects on synaptic density measures (V_T).³³ Our previous study in AD demonstrated broad regional differences in K_1 in temporoparietal cortices relative to CN,¹¹ similar to the pattern of known cortical hypometabolism in AD. Similar concepts have been investigated previously in the early dynamic flow images of PET with amyloid tracers.^{68–70} The high correlations between relative perfusion (R_1) and metabolism (K_iR) across all the susceptible regions further supported the similarity between those measures (Figure 5 and Table S6). We may be able to take advantage of this feature to gather useful information of both neuronal activity from K_1 or R_1 perfusion imaging and synaptic density from V_T or DVR parametric images within a single [¹¹C]UCB-J PET study.

Absolute and normalized outcome measures

In this study, we evaluated both absolute measures (K_1 , V_T for [¹¹C]UCB-J and K_i for [¹⁸F]FDG) and normalized measures to reference regions (R_1 , DVR , for [¹¹C]UCB-J and K_iR for [¹⁸F]FDG) for differentiation between AD and CN. It is critical to understand the pros and cons of absolute and normalized measures. Absolute measures are directly derived from kinetic

modeling methods using input functions (i.e., arterial sampling for [^{11}C]UCB-J and PBIF for [^{18}F]FDG). Normalized measures require the availability of a suitable reference tissue/regions, usually devoid of specific binding (e.g., white matter) or having no effect from disease (e.g. cerebellum for AD). The absolute measures provide direct estimation of physiology but require arterial blood sampling and often have higher inter-subject variability (e.g., due to noise in the measurement of the input function) and therefore less sensitivity for detecting group differences. In contrast, normalized measures provide a relative estimate of physiology and usually have less inter-subject variability and higher sensitivity for detecting group differences. It is important to recognize that normalized measures could artifactually contribute to higher, positive correlations between [^{11}C]UCB-J and [^{18}F]FDG simply due to using the same cerebellum reference. Also, small numerical differences in reference region values could contribute inappropriately to the detection of group differences. Here, we observed lower, albeit nonsignificant, [^{11}C]UCB-J K_1 (PD:2.3%) and V_T (PD:2.7%) in the cerebellum of AD compared to CN in this study, which was more than our previous studies (<1% differences),^{11,12} which potentially underestimated the between-group differences of [^{11}C]UCB-J R_1 and DVR after normalization. In contrast, we observed a slightly higher (again nonsignificant) [^{18}F]FDG K_i (4.2%) in the cerebellum of AD compared to CN, which potentially overestimated the PD in regional hypometabolism (K_iR) post normalization.

Limitations

This study has a number of limitations. First, it has a moderate sample size ($n = 25$) with small differences of sex and education years between AD and CN groups. In addition, we did not include sex, education level, or age variates in the linear mixed model analysis due to both the small sample size and the fact that we focused on the within-subject comparison between SV2A and [^{18}F]FDG PET. As we recruit more AD participants for studies with multiple tracers, we hope to provide a better comparison between SV2A and [^{18}F]FDG PET in the future. Methodologically, M-G PVC may not be an ideal method of correcting partial volume effects for both SV2A PET and [^{18}F]FDG and might introduce uncertainty in the data of the current study. We are currently exploring other PVC methods including the iterative Yang approach for SV2A.⁷¹ Arterial blood sampling for SV2A PET is a cumbersome procedure for participants and limits the utility of this method for multi-center or longitudinal studies. Importantly, we have recently demonstrated that simpler SUVR measures are valid for SV2A-PET.⁷²

Conclusion

We have presented the first comparison study for [^{11}C]UCB-J for synaptic density and [^{18}F]FDG metabolism for functional neuronal activity and have demonstrated distinct regional patterns in the same AD participants. The critical measures of synaptic loss and hypoperfusion/hypometabolism are likely to be complementary for understanding the pathophysiology of AD, and both can be obtained with a single dynamic [^{11}C]UCB-J PET scan.

Funding

The author(s) disclosed receipt of the following financial support for the research, authorship, and/or publication of this article: The Dana Foundation David Mahoney Neuroimaging Grant, Pilot grant of Yale Alzheimer's Disease Research Center NIH P50AG047270, NIH R01AG52560, NIH R01AG062276, NIH K23AG057784, NIH T32MH019961-21A1, Research grant from Eli Lilly.

Acknowledgements

We thank all study participants, as well as the staff from the Yale Alzheimer's Disease Research Unit and the Yale PET Center for their expert assistance. We thank UCB Pharma in Brussels Belgium for providing the [^{11}C]UCB-J radiolabeling precursor and reference standard.

Declaration of conflicting interests

The author(s) declared the following potential conflicts of interest with respect to the research, authorship, and/or publication of this article: MKC reports research support from the Dana Foundation and Eli Lilly for the conduct of the study. APM, REC, and CHvD report grants from National Institutes of Health for the conduct of the study. MKC reports consulting fees from Eisai and Actinium and clinical trial of Merck outside the submitted work. APM reports grants for clinical trials from Genentech and Eisai outside the submitted work. YH reports research grants from the UCB and Eli Lilly outside the submitted work. YH, NBN, and REC have a patent for a newer version of the tracer. REC is a consultant for Rodin Therapeutics and has received research funding from UCB. REC reports having received grants from AstraZeneca, Astellas, Eli Lilly, Pfizer, Taisho, and UCB, outside the submitted work. CHvD reports consulting fees from Kyowa Kirin, Roche, Merck, Eli Lilly, and Janssen and grants for clinical trials from Biogen, Novartis, Eli Lilly, Merck, Eisai, Janssen, Roche, Genentech, Toyama, and Biohaven, outside the submitted work. No other disclosures are reported.

Authors' contributions





M-KC, REC, and CHV were responsible for the concept and design of the study. M-KC, APM, AFTA, REC, and CHV were responsible for literature search, data and imaging interpretation. M-KC was responsible for drafting of the original report, figures and tables., which was reviewed and revised by

all coauthors. APM, JWM, HRM, and CHV were responsible for recruiting participants, acquisition of MRI scans, and clinical assessments. NBN, and YH were responsible for the synthesis of UCB-J radiotracers. M-KC, APM, REC, and CHV were responsible for acquisition of PET data. S-FL was responsible for metabolite analysis and arterial input function. APM, MN, SJF, TT, RO and JM were responsible for PET imaging analyses. M-KC, APM, and BVW were responsible for statistical analysis. Funding was obtained by M-KC, REC, and CHV. M-KC the first and corresponding author had full access to all the data in the study and takes responsibility for the integrity of the data and the accuracy of the data analysis.

Supplementary material

Supplemental material for this article is available online.

ORCID iDs

Mika Naganawa  <https://orcid.org/0000-0002-4408-2621>
 Jayanta Mondal  <https://orcid.org/0000-0002-2387-7054>
 Sjoerd J Finnema  <https://orcid.org/0000-0002-4972-3627>
 Nabeel B Nabulsi  <https://orcid.org/0000-0001-8129-0051>

References

- Jack CR Jr, Bennett DA, Blennow K, et al.; Contributors. NIA-AA research framework: toward a biological definition of Alzheimer's disease. *Alzheimers Dement* 2018; 14: 535–562.
- Jack CR Jr, Bennett DA, Blennow K, et al. A/T/N: an unbiased descriptive classification scheme for Alzheimer disease biomarkers. *Neurology* 2016; 87: 539–547.
- Klunk WE, Engler H, Nordberg A, et al. Imaging brain amyloid in Alzheimer's disease with Pittsburgh Compound-B. *Ann Neurol* 2004; 55: 306–319.
- Barthel H and Sabri O. Clinical use and utility of amyloid imaging. *J Nucl Med* 2017; 58: 1711–1717.
- Betthausen TJ, Cody KA, Zammit MD, et al. In vivo characterization and quantification of neurofibrillary tau PET radioligand [(18)F]MK-6240 in humans from Alzheimer's disease dementia to young controls. *J Nucl Med* 2019; 60: 93–99.
- Johnson KA, Schultz A, Betensky RA, et al. Tau positron emission tomographic imaging in aging and early Alzheimer disease. *Ann Neurol* 2016; 79: 110–119.
- Mosconi L. Glucose metabolism in normal aging and Alzheimer's disease: methodological and physiological considerations for PET studies. *Clin Transl Imaging* 2013; 1: 217–233
- Bailly M, Destrieux C, Hommet C, et al. Precuneus and cingulate cortex atrophy and hypometabolism in patients with Alzheimer's disease and mild cognitive impairment: MRI and (18)F-FDG PET quantitative analysis using FreeSurfer. *Biomed Res Int* 2015; 2015: 1–09.
- Chetelat G, Desgranges B, Landeau B, et al. Direct voxel-based comparison between grey matter hypometabolism and atrophy in Alzheimer's disease. *Brain* 2008; 131: 60–71.
- Ishii K, Sasaki H, Kono AK, et al. Comparison of gray matter and metabolic reduction in mild Alzheimer's disease using FDG-PET and voxel-based morphometric MR studies. *Eur J Nucl Med Mol Imaging* 2005; 32: 959–963.
- Chen MK, Mecca AP, Naganawa M, et al. Assessing synaptic density in Alzheimer disease with synaptic vesicle glycoprotein 2A positron emission tomographic imaging. *JAMA Neurol* 2018; 75: 1215–1224.
- Mecca AP, Chen MK, O'Dell RS, et al. In vivo measurement of widespread synaptic loss in Alzheimer's disease with SV2A PET. *Alzheimers Dement* 2020; 16: 974–982.
- Arbizu J, Festari C, Altomare D, et al.; EANM-EAN Task Force for the Prescription of FDG-PET for Dementing Neurodegenerative Disorders. Clinical utility of FDG-PET for the clinical diagnosis in MCI. *Eur J Nucl Med Mol Imaging* 2018; 45: 1497–1508.
- Drzezga A, Altomare D, Festari C, et al.; EANM-EAN Task Force for the Prescription of FDG-PET for Dementing Neurodegenerative Disorders. Diagnostic utility of 18F-Fluorodeoxyglucose positron emission tomography (FDG-PET) in asymptomatic subjects at increased risk for Alzheimer's disease. *Eur J Nucl Med Mol Imaging* 2018; 45: 1487–1496.
- Landau SM, Harvey D, Madison CM, et al.; Alzheimer's Disease Neuroimaging Initiative. Associations between cognitive, functional, and FDG-PET measures of decline in AD and MCI. *Neurobiol Aging* 2011; 32: 1207–1218.
- Nestor PJ, Altomare D, Festari C, et al.; EANM-EAN Task Force for the Prescription of FDG-PET for Dementing Neurodegenerative Disorders. Clinical utility of FDG-PET for the differential diagnosis among the main forms of dementia. *Eur J Nucl Med Mol Imaging* 2018; 45: 1509–1525.
- Chamberlain S, Gabriel H, Strittmatter W, et al. An exploratory phase IIa study of the PPAR Delta/gamma agonist T3D-959 assessing metabolic and cognitive function in subjects with mild to moderate Alzheimer's disease. *J Alzheimers Dis* 2020; 73: 1085–1103.
- van Dyck CH, Nygaard HB, Chen K, et al. Effect of AZD0530 on cerebral metabolic decline in Alzheimer disease: a randomized clinical trial. *JAMA Neurol* 2019; 76: 1219.
- Wiers CE, Shokri-Kojori E, Wong CT, et al. Cannabis abusers show hypofrontality and blunted brain responses to a stimulant challenge in females but not in males. *Neuropsychopharmacology* 2016; 41: 2596–2605.
- Teipel SJ, Drzezga A, Bartenstein P, et al. Effects of donepezil on cortical metabolic response to activation during (18)FDG-PET in Alzheimer's disease: a double-blind cross-over trial. *Psychopharmacology (Berl)* 2006; 187: 86–94.
- Ishibashi K, Onishi A, Fujiwara Y, et al. Relationship between Alzheimer disease-like pattern of 18F-FDG and fasting plasma glucose levels in cognitively normal volunteers. *J Nucl Med* 2015; 56: 229–233.
- Burns CM, Chen K, Kaszniak AW, et al. Higher serum glucose levels are associated with cerebral

- hypometabolism in Alzheimer regions. *Neurology* 2013; 80: 1557–1564.
23. Brooks RA, Di Chiro G, Zukerberg BW, et al. Test-retest studies of cerebral glucose metabolism using fluorine-18 deoxyglucose: validation of method. *J Nucl Med* 1987; 28: 53–59.
 24. Schmidt ME, Ernst M, Matochik JA, et al. Cerebral glucose metabolism during pharmacologic studies: test-retest under placebo conditions. *J Nucl Med* 1996; 37: 1142–1149.
 25. Shiyam Sundar LK, Muzik O, Rischka L, et al. Promise of fully integrated PET/MRI: Noninvasive clinical quantification of cerebral glucose metabolism. *J Nucl Med* 2020; 61: 276–284.
 26. Bajjalieh SM, Frantz GD, Weimann JM, et al. Differential expression of synaptic vesicle protein 2 (SV2) isoforms. *J Neurosci* 1994; 14: 5223–5235.
 27. Bajjalieh SM, Peterson K, Linial M, et al. Brain contains two forms of synaptic vesicle protein 2. *Proc Natl Acad Sci USA* 1993; 90: 2150–2154.
 28. Mutch SA, Kensel-Hammes P, Gadd JC, et al. Protein quantification at the single vesicle level reveals that a subset of synaptic vesicle proteins are trafficked with high precision. *J Neurosci* 2011; 31: 1461–1470.
 29. Holmes SE, Scheinost D, Finnema SJ, et al. Lower synaptic density is associated with depression severity and network alterations. *Nat Commun* 2019; 10: 1529–1504.
 30. Onwordi EC, Half EF, Whitehurst T, et al. Synaptic density marker SV2A is reduced in schizophrenia patients and unaffected by antipsychotics in rats. *Nat Commun* 2020; 11: 246–201.
 31. Matuskey D, Tinaz S, Wilcox KC, et al. Synaptic changes in Parkinson disease assessed with in vivo imaging. *Ann Neurol* 2020; 87: 329–338.
 32. Finnema SJ, Nabulsi NB, Mercier J, et al. Kinetic evaluation and test-retest reproducibility of [(11)C]UCB-J, a novel radioligand for positron emission tomography imaging of synaptic vesicle glycoprotein 2A in humans. *J Cereb Blood Flow Metab* 2018; 38: 2041–2052.
 33. Smart K, Liu H, Matuskey D, et al. Binding of the synaptic vesicle radiotracer [(11)C]UCB-J is unchanged during functional brain activation using a visual stimulation task. *J Cereb Blood Flow Metab* 2020. Epub ahead of print 8 August 2020. DOI: 10.1177/0271678x20946198.
 34. Finnema SJ, Rossano S, Naganawa M, et al. A single-center, open-label positron emission tomography study to evaluate brivaracetam and levetiracetam synaptic vesicle glycoprotein 2A binding in healthy volunteers. *Epilepsia* 2019; 60: 958–967.
 35. Nabulsi NB, Mercier J, Holden D, et al. Synthesis and preclinical evaluation of ¹¹C-UCB-J as a PET tracer for imaging the synaptic vesicle glycoprotein 2A in the brain. *J Nucl Med* 2016; 57: 777–784.
 36. Rossano S, Toyonaga T, Finnema SJ, et al. Assessment of a white matter reference region for (11)C-UCB-J PET quantification. *J Cereb Blood Flow Metab* 2020; 40: 1890–1901.
 37. de Wilde MC, Overk CR, Sijben JW, et al. Meta-analysis of synaptic pathology in Alzheimer's disease reveals selective molecular vesicular machinery vulnerability. *Alzheimers Dement* 2016; 12: 633–644.
 38. Patlak CS, Blasberg RG and Fenstermacher JD. Graphical evaluation of blood-to-brain transfer constants from multiple-time uptake data. *J Cereb Blood Flow Metab* 1983; 3: 1–7.
 39. Naganawa M, Gallezot JD, Shah V, et al. Assessment of population-based input functions for patlak imaging of whole body dynamic (18)F-FDG PET. *EJNMMI Phys* 2020; 7: 67–11.
 40. Malone IB, Leung KK, Clegg S, et al. Accurate automatic estimation of total intracranial volume: a nuisance variable with less nuisance. *Neuroimage* 2015; 104: 366–372.
 41. Mecca AP, Barcelos NM, Wang S, et al. Cortical beta-amyloid burden, gray matter, and memory in adults at varying APOE epsilon4 risk for Alzheimer's disease. *Neurobiol Aging* 2018; 61: 207–214.
 42. Muller-Gartner HW, Links JM, Prince JL, et al. Measurement of radiotracer concentration in brain gray matter using positron emission tomography: MRI-based correction for partial volume effects. *J Cereb Blood Flow Metab* 1992; 12: 571–583.
 43. Weaver B and Wuensch KL. SPSS and SAS programs for comparing Pearson correlations and OLS regression coefficients. *Behav Res Methods* 2013; 45: 880–895.
 44. Minoshima S. A diagnostic approach in Alzheimer's disease using three-dimensional stereotactic surface projections of fluorine-18-FDG PET. *J Nucl Med* 1978; 36: 1238–1248.
 45. Minoshima S, Foster NL and Kuhl DE. Posterior cingulate cortex in Alzheimer's disease. *Lancet* 1994; 344: 895.
 46. Villain N, Desgranges B, Viader F, et al. Relationships between hippocampal atrophy, white matter disruption, and gray matter hypometabolism in Alzheimer's disease. *J Neurosci* 2008; 28: 6174–6181.
 47. Chen Y, Wolk DA, Reddin JS, et al. Voxel-level comparison of arterial spin-labeled perfusion MRI and FDG-PET in Alzheimer disease. *Neurology* 2011; 77: 1977–1985.
 48. Yakushev I, Schreckenberger M, Müller MJ, et al. Functional implications of hippocampal degeneration in early Alzheimer's disease: a combined DTI and PET study. *Eur J Nucl Med Mol Imaging* 2011; 38: 2219–2227.
 49. Ossenkoppele R, Schonhaut DR, Schöll M, et al. Tau PET patterns mirror clinical and neuroanatomical variability in Alzheimer's disease. *Brain* 2016; 139: 1551–1567.
 50. Hanseeuw BJ, Betensky RA, Schultz AP, et al. Fluorodeoxyglucose metabolism associated with tau-amyloid interaction predicts memory decline. *Ann Neurol* 2017; 81: 583–596.
 51. Adams JN, Lockhart SN, Li L, et al. Relationships between tau and glucose metabolism reflect Alzheimer's disease pathology in cognitively normal older adults. *Cereb Cortex* 2019; 29: 1997–2009.
 52. Bischof GN, Jessen F, Fliessbach K, et al.; Alzheimer's Disease Neuroimaging Initiative. Impact of tau and amyloid burden on glucose metabolism in Alzheimer's disease. *Ann Clin Transl Neurol* 2016; 3: 934–939.

53. Albrecht D, Isenberg AL, Stradford J, et al. Associations between vascular function and tau PET are associated with global cognition and amyloid. *J Neurosci* 2020; 40: 8573–8586.
54. Carrera E and Tononi G. Diaschisis: past, present, future. *Brain* 2014; 137: 2408–2422.
55. Braak H, Thal DR, Ghebremedhin E, et al. Stages of the pathologic process in Alzheimer disease: age categories from 1 to 100 years. *J Neuropathol Exp Neurol* 2011; 70: 960–969.
56. Gomez-Isla T, West HL, Rebeck GW, et al. Clinical and pathological correlates of apolipoprotein E e4 in Alzheimer's disease. *Ann Neurol* 1996; 39: 62–70.
57. Meguro K, Blaizot X, Kondoh Y, et al. Neocortical and hippocampal glucose hypometabolism following neurotoxic lesions of the entorhinal and perirhinal cortices in the non-human primate as shown by PET: implications for Alzheimer's disease. *Brain* 1999; 122: 1519–1531.
58. Cunnane S, Nugent S, Roy M, et al. Brain fuel metabolism, aging, and Alzheimer's disease. *Nutrition* 2011; 27: 3–20.
59. Merlini M, Meyer EP, Ulmann-Schuler A, et al. Vascular β -amyloid and early astrocyte alterations impair cerebrovascular function and cerebral metabolism in transgenic arcA β mice. *Acta Neuropathol* 2011; 122: 293–311.
60. Morita M, Ikeshima-Kataoka H, Kreft M, et al. Metabolic plasticity of astrocytes and aging of the brain. *Ijms* 2019; 20: 941.
61. Zimmer ER, Parent MJ, Souza DG, et al. (18)F]FDG PET signal is driven by astroglial glutamate transport. *Nat Neurosci* 2017; 20: 393–395.
62. Huang CW, Hsu SW, Chang YT, et al. Cerebral perfusion insufficiency and relationships with cognitive deficits in Alzheimer's disease: a multiparametric neuroimaging study. *Sci Rep* 2018; 8: 1541–1501.
63. Arendt T. Synaptic degeneration in alzheimer's disease. *Acta Neuropathol* 2009; 118: 167–179. 2009/04/25. DOI: 10.1007/s00401-009-0536-x.
64. DeKosky ST and Scheff SW. Synapse loss in frontal cortex biopsies in Alzheimer's disease: correlation with cognitive severity. *Ann Neurol* 1990; 27: 457–464.
65. Snow AD, Nochlin D, Sekiguchi R, et al. Identification and immunolocalization of a new class of proteoglycan (keratan sulfate) to the neuritic plaques of Alzheimer's disease. *Exp Neurol* 1996; 138: 305–317.
66. Rocher AB, Chapon F, Blaizot X, et al. Resting-state brain glucose utilization as measured by PET is directly related to regional synaptophysin levels: a study in baboons. *Neuroimage* 2003; 20: 1894–1898.
67. Aalst JV, Ceccarini J, Sunaert S, et al. In vivo synaptic density relates to glucose metabolism at rest in healthy subjects, but is strongly modulated by regional differences. *J Cereb Blood Flow Metab*. Epub ahead of print. DOI: 10.1177/0271678x20981502.
68. Kadir A, Almkvist O, Forsberg A, et al. Dynamic changes in PET amyloid and FDG imaging at different stages of Alzheimer's disease. *Neurobiol Aging* 2012; 33: 198.e191–114.
69. Meyer PT, Hellwig S, Amtage F, et al. Dual-biomarker imaging of regional cerebral amyloid load and neuronal activity in dementia with PET and 11C-labeled Pittsburgh compound B. *J Nucl Med* 2011; 52: 393–400.
70. Rodriguez-Vieitez E, Carter SF, Chiotis K, et al. Comparison of early-phase 11C-deuterium-l-deprenyl and 11C-Pittsburgh compound B PET for assessing brain perfusion in Alzheimer disease. *J Nucl Med* 2016; 57: 1071–1077.
71. Erlandsson K, Buvat I, Pretorius PH, et al. A review of partial volume correction techniques for emission tomography and their applications in neurology, cardiology and oncology. *Phys Med Biol* 2012; 57: R119–159.
72. Naganawa M, Gallezot JD, Finnema S, et al. Simplified quantification of (11)C-UCB-J PET evaluated in a large human cohort. *J Nucl Med* 2021; 62: 418–407.